Revealing phase transition in dense matter with gravitational wave spectroscopy of binary neutron star mergers

Pedro L. Espino,[1,2] Aviral Prakash,[1,3] David Radice,[1,3,4] and Domenico Logoteta[5,6,7,8]

[1]*Institute for Gravitation & the Cosmos, The Pennsylvania State University, University Park, Pennsylvania 16802, USA*
[2]*Department of Physics, University of California, Berkeley, California 94720, USA*
[3]*Department of Physics, The Pennsylvania State University, University Park, Pennsylvania 16802, USA*
[4]*Department of Astronomy & Astrophysics, The Pennsylvania State University, University Park, Pennsylvania 16802, USA*
[5]*Dipartimento di Fisica, Università di Pisa, Largo B. Pontecorvo, 3 I-56127 Pisa, Italy*
[6]*INFN, Sezione di Pisa, Largo B. Pontecorvo, 3 I-56127 Pisa, Italy*
[7]*Dipartimento di Fisica, Universitá di Trento, Via Sommarive 14, 38123 Trento, Italy*
[8]*INFN-TIFPA, Trento Institute for Fundamental Physics and Applications, via Sommarive 14, I-38123 Trento, Italy*

(Received 29 May 2023; accepted 2 May 2024; published 4 June 2024)

We use numerical relativity simulations of binary neutron star mergers to show that high density deconfinement phase transitions to quark matter can be probed using multimodal postmerger gravitational wave (GW) spectroscopy. Our simulations suggest that hadron-quark phase transitions may suppress the one-armed spiral instability in the remnant. This is manifested in an anticorrelation between the energy carried in the $\ell = 2$, $m = 1$ GW mode and energy density gap which separates the two phases. Our work demonstrates a potential connection between features of the postmerger GW spectrum and microphysical features of the high-density equation of state.

DOI: 10.1103/PhysRevD.109.123009

I. INTRODUCTION

Binary neutron star (BNS) mergers produce some of the most extreme conditions in nature, compressing matter to several times the nuclear density and to temperatures of tens of MeV [1]. More extreme conditions are only found in the early Universe and in the interior of black holes. Multimessenger observations of BNS mergers can be used to probe the properties of matter in these conditions, providing a unique avenue to study the nonperturbative regime of QCD [2–27].

Presently, there are large uncertainties in the fundamental physics of strongly interacting matter at densities of a few times nuclear saturation [28–30]. It is not even clear what the relevant degrees of freedom are for the densities and temperatures reached in the core of remnant massive neutron stars (RMNS) of BNS mergers. It is possible that matter remains composed of nucleons, together with leptons (electrons, positrons, and muons) and photons [1,31]. The appearance of more exotic baryons, such as hyperons, is not excluded [5,8,32]. It is also possible for a transition to the deconfined quark-gluon plasma phase to take place in BNS mergers [13–15,27]. The determination of the state of matter formed in BNS mergers is one of the most pressing scientific objectives of multimessenger astronomy [33,34].

Previous work has shown that the presence of phase transitions (PTs) to deconfined quarks can be revealed by a shift of the postmerger gravitational wave (GW) peak frequency f_2 from the value expected for hadronic equations of state (EOSs) [15,35–37]. However, such frequency shifts can be degenerate with deviations from universal relations due to hadronic physics or other effects [13,26,27,35,38,39]. It has also been suggested that the presence of a PT could be inferred from a measurement of the threshold mass for prompt collapse of BNS systems [24,25,40,41]. In this work, we consider 14 state-of-the-art numerical relativity simulations to show, for the first time, that the presence and strength of a QCD PT could be unambiguously determined through multimodal GW spectroscopy of RMNS. Such measurements will be possible with the next-generation of GW experiments like Cosmic Explorer [42], Einstein Telescope [43], and NEMO [44]. We vary many system properties including the mass ratio, eccentricity, and EOS model. Crucially, our simulations employ EOS models which cover a wide range of features for the PT, including different constructions and energy density gaps separating the two phases. The remainder of the paper is organized as follows. In Sec. II we discuss the features of the EOS models we consider, with particular focus on a quantity that measures the effective "strength" of the PT. In Sec. III we discuss our numerical methods and discuss the construction of the initial data for our simulations. In Sec. IV we detail our main results and discuss the use of multimodal GW spectroscopy as a tool for

understanding the nuclear structure of the NS EOS. Finally, we conclude in Sec. V and discuss future directions of investigation. Throughout the work we assume geometrized units, with $G = c = 1$, unless otherwise stated.

II. EQUATION OF STATE MODELS

For a clear understanding of the role that high-density deconfinement PTs could play in the development of the one-arm spiral instability, we consider a total of six EOS models and run a total of ten simulations with varying PT features. In particular, the size of the energy density gap which separates the hadronic and quark phases is a useful way to classify hybrid hadron-quark EOS models and provides a qualitative measure of the "strength" of the phase transition [45]. For example, EOS models that use smaller energy gaps tend to produce more gradual effects such as a small "softening" (i.e., a relative lowering of the pressure when compared to purely hadronic EOS models) at high densities, whereas EOS models which use larger energy gaps can produce more drastic effects such as the production of a disjoint third branch of compact stars, separated from the neutron star branch by a sequence of unstable equilibria [45]. Key relevant parameters for describing the nature of EOS models with deconfinement PTs are the energy density and pressure corresponding to the onset of the transition $\epsilon_{\rm trans}$ and $p_{\rm trans}$, respectively, such that fluid elements with pressure and energy densities above this are expected to be in the mixed or pure quark phase. Also important is the gap in energy density which separates the pure hadronic and pure quark phases [45]

$$\Delta\epsilon \equiv \epsilon_{\rm quark} - \epsilon_{\rm trans}, \tag{1}$$

where $\epsilon_{\rm quark}$ is the energy density above which the EOS describes pure quark matter. In principle, the parameters $\epsilon_{\rm trans}$, $p_{\rm trans}$, and $\Delta\epsilon$ are functions of the electron fraction $Y_{\rm e}$ and temperature T, but for simplicity we assume that the values of these quantities are those for cold ($T \lesssim 1$ MeV), β-equilibrated matter when discussing them. We identify the end and beginning of each phase by considering the change in the approximate adiabatic index $\Gamma = {\rm d}\log p/{\rm d}\log(\rho)$, where p and ρ are the fluid pressure and rest mass density, respectively, of the cold, β-equilibrium, barotropic EOS for each EOS model considered. The region corresponding to the PT is always unambiguously marked by discontinuities in, or sudden changes in the slope of, the adiabatic index for the EOS models we consider.

In Table I we list the relevant details of the EOS models considered in our work, along with references to literature where the models are described in further detail or used in general relativistic hydrodynamics (GRHD) simulations. We consider EOS models that cover several sizes of the energy density gap, ranging from nonexistent (i.e., a purely hadronic EOS) to significantly large (such that the aforementioned more "drastic" effects on the sequence of stable stars is achieved), while maintaining consistency with current astrophysical constraints on the dense matter EOS. We consider both phenomenological EOS models [46–50] (in the form of piecewise polytropic approximations [51], abbreviated in Table I as "PP") and microphysical, finite temperature EOS models [27,52–54] (abbreviated in Table I as "FT"). In simulations that employ piecewise polytropic approximations to the EOS, we consider a thermal treatment via the standard Γ-law EOS with thermal adiabatic index $\Gamma_{\rm th} = 1.8$. While a finer sampling of the $\Delta\epsilon$ parameter space would provide a more extensive study, the design of new EOS models consistent with astrophysical observations of NS properties was outside the scope of this work. As such, we considered as wide a range in $\Delta\epsilon$ as possible considering existing and available EOS models. We leave the exploration of a wider and more finely sampled (in $\Delta\epsilon$) EOS model space to future work.

TABLE I. Summary of key properties for the EOS models considered in this work. We list the EOS model name, relevant degrees of freedom (d.o.f.) considered (with h and q standing for hadrons and quarks, respectively), energy density gap $\Delta\epsilon$ in units of 10^{15} g cm^{-3}, type of EOS considered (where "PP" stands for piecewise polytropic and "T" stands for a tabulated EOS model; all PP and T type EOS models consider a Γ-law EOS with $\Gamma = 1.8$ and microphysical finite temperature thermal EOS treatment, respectively), and literature reference with further details on the model (Ref.). For EOS models that include a deconfinement PT to quark matter, we also list the counterpart hadronic EOS which is identical to the model below the threshold densities for quark deconfinement (Count).

EOS	d.o.f.	$\Delta\epsilon$	Type	Ref.	Counterpart
BLh	h	0.0	T	[27,53,54]	–
DD2F	h	0.0	T	[27,52]	–
DD2F-SF1	h-q	0.1967	T	[27,52]	DD2F
DD2F-SF5	h-q	0.1967	T	[27,52]	DD2F
BBKF1.5	h-q	0.2048	PP	–	DD2F
BLQ	h-q	0.319	T	[27,53,54]	BLh
T9	h-q	0.5922	PP	[46–50]	DD2FPP

III. METHODS

We consider binaries in both quasicircular orbits and highly eccentric encounters on nearly parabolic orbits. Initial data for the quasicircular binaries is created using the conformal thin sandwich formalism [55] and assuming a helical Killing vector and irrotational flows. The resulting elliptic equations are solved using the pseudospectral code LORENE [56–58]. Initial data for the eccentric encounters is constructed by superimposing two isolated, boosted, neutron stars (NSs), following [59]. The initial separation of the stellar barycenters for parabolic encounters is set to 100 km, which is sufficiently large so that the level of constraint violation in the initial data is comparable to that of the quasicircular binaries.

We perform NS merger simulations using the WhiskyTHC code [60–62]. WhiskyTHC makes use of the CTGamma spacetime solver [63], which is a part of the Einstein Toolkit [64]. The adaptive mesh refinement driver Carpet [65] is used to generate the dynamical grid structure employed in the simulations. All simulations considered here, with the exception of two, have been performed using at least two grid resolutions. Although there are small quantitative differences in the GW waveforms computed at different resolutions, the effects of PTs on the GW spectrum discussed here are robust across all simulations. Unless otherwise specified, we discuss results from simulations using the standard grid resolution (SR) (with grid spacing $\Delta x \simeq$ 184.6 m in the finest refinement level). The grid for lower resolution (LR) simulations is approximately 30% coarser than that of our SR grids. The grid structure for the simulations is the same adapted in [59] and [66]) for the quasicircular and eccentric simulations, respectively. Neutrino emission and reabsorption are not included for binaries in eccentric orbits. All quasicircular binaries include a neutrino treatment via the moment based M0 scheme [66]. Additionally, magnetic fields are not accounted for in any of our simulations, although all simulations account for angular momentum transport in the postmerger RMNS with the use of a subgrid viscosity large eddy simulation model that remains fixed across models.

The complete set of simulations considered in this work cover a wide variety of initial conditions and modeling assumptions. To further clarify the conditions considered we summarize in Table II the initial conditions and modeling assumptions that vary across the simulations. We note that several of the variable modeling assumptions are not expected to influence the development of the dynamics of the RMNS on the timescales we consider, including the use of an M0 neutrino scheme [67,68] and the eccentricity of the orbit. The most relevant model assumptions are the subgrid viscosity large eddy simulation model and the mass ratio. Specifically, the use of a subgrid viscosity model accounts for angular momentum transport in the RMNS, which largely dictates the differential rotation profile crucial for the development of the one-armed spiral instability [69]. Moreover, the use of nonunity mass-ratio ensures an inherent perturbation in the system that reliably seeds the one-armed spiral instability. We emphasize that the important modeling assumptions, including the subgrid viscosity model and mass ratio (with the exception of a single pair of simulations to understand the effects of mass ratio), remain fixed across all of our simulations. We also emphasize that our main focus is the relative growth of the one-armed spiral instability in each pair of simulations and that we only compare simulations with identical initial conditions and modeling assumptions. The only difference between the pairs of simulations which we compare is whether the EOS includes a deconfinement phase transition or not. From this perspective, all potential modeling differences across our simulations should in principle not play a role in the effects we report.

TABLE II. Summary of the modeling assumption and initial conditions for the simulations considered in this work. We list the EOS, relevant d.o.f. modeled in the EOS (with h and q standing for hadrons and quarks, respectively), orbital condition imposed, neutrino model assumed, grid resolutions considered, total system mass, and mass ratio $q = M_1/M_2$ [where M_1 (M_2) is the mass of the less (more) massive star in the configuration].

EOS	d.o.f.	Orbit	ν	Resolution	$M(M_\odot)$	q
BLh	h	Quasicircular	M0	LR/SR	2.6	1
BLh	h	Quasicircular	M0	SR	2.6	0.85
DD2F	h	Quasicircular	M0	LR/SR	2.6	1
DD2F	h	Quasicircular	M0	LR/SR	2.7	1
DD2F	h	Eccentric	–	LR/SR	2.7	1
DD2F-SF1	h-q	Quasicircular	M0	LR/SR	2.6	1
DD2F-SF1	h-q	Quasicircular	M0	LR/SR	2.7	1
DD2F-SF5	h-q	Eccentric	–	LR/SR	2.7	1
BBKF1.5	h-q	Eccentric	–	LR/SR	2.7	1
BLQ	h-q	Quasicircular	M0	LR/SR	2.6	1
BLQ	h-q	Quasicircular	M0	SR	2.6	0.85
T9	h-q	Eccentric	–	LR/SR	2.7	1

IV. RESULTS

A. Development of the one-armed spiral instability in BNS mergers

The one-armed spiral instability is a nonaxisymmetric mode in a rapidly rotating fluid which, when saturated, leads to the dominance of a single high-density mode in the fluid density that is displaced from the fluid barycenter [70–73]. The one-armed spiral instability has been observed to develop commonly in BNS merger simulations that produce long-lived, massive postmerger remnants on timescales of $\mathcal{O}(10\ \mathrm{ms})$ [74–78] and in simulations of many other astrophysical systems including supernovae [79,80], white dwarfs [81,82], and accretion disks [82,83].

A unique feature of the one-arm spiral mode is that it can be sustained on significantly longer timescales than other nonaxisymmetric modes. In the context of BNS mergers, the growth and saturation of the one-arm spiral mode may be numerically observed by considering azimuthal decompositions of the rest mass density on the orbital plane. Specifically, we consider the amplitudes of these rest mass density decompositions as

$$C_m = \int W \sqrt{\gamma} \rho e^{-im\phi} \mathrm{d}x\mathrm{d}y, \tag{2}$$

where W is the Lorentz factor, γ is the determinant of the three metric, ρ is the rest mass density, and $\phi = \tan^{-1}(y/x)$ is the azimuthal angle in the center of mass frame. An indicative dynamical probe of the growth of the one-arm

spiral instability is the dominance of the C_1 mode over the typically initially dominant C_2 mode. On dynamical timescales the one-arm instability leads to the growth of the C_1 density mode, while the C_2 mode simultaneously decays.

Each fluid density mode that arises during the evolution of a massive NS remnant is associated with GW emission at a characteristic frequency stemming from its respective pattern speed. For example, the growth of the C_1 mode, which has half the pattern frequency as the C_2 mode, is associated with GW emission at half the characteristic frequency of the initially dominant C_2 mode. As such, the development of the one-armed spiral instability in astrophysical systems may be observed by considering multimodal GW spectroscopy [77]. For the simulations considered in this work we extract multimodal GW information within the Newman-Penrose formalism. We compute the coefficients of $s=-2$ spin-weighted spherical harmonic decompositions of the Newman-Penrose scalar Ψ_4, which we label as $\Psi_4^{l,m}$. The one-armed spiral instability can therefore be observed in the GW spectrum extracted from our simulations as a growth in the power and amplitude of the $\ell=2$, $m=1$ GW mode (i.e., $\Psi_4^{2,1}$) and simultaneous decay of the dominant $\ell=2$, $m=2$ GW mode (i.e., $\Psi_4^{2,2}$).

B. The effect of deconfinement phase transitions on the one-armed spiral instability

Our simulations show that high-density deconfinement PTs may act to suppress the one-armed spiral instability. Specifically, hadron-quark PTs lead to a relative suppression of the instability when compared to analogous cases with purely hadronic degrees of freedom. We refer to this effect simply as a "relative suppression" throughout the manuscript for the sake of brevity. There are several potential mechanisms via which the instability may be relatively suppressed. For example, it has been shown that the physical extent of the remnant plays an important role in the development of the instability, with larger remnants being more conducive to the development of the instability on shorter timescales [77,78,84,85]. The significant softening at high densities introduced by the PT results in more compact postmerger remnants (relative to scenarios that consider only hadronic degrees of freedom). As such, the more compact hybrid star remnants may see a weaker development of the one-armed spiral instability when compared to neutron star remnants.

In Fig. 1 we depict the density mode decomposition for two representative simulations which begin from the same initial conditions. The left and right panel of Fig. 1 depict the dominant density modes for a simulation employing a hadronic (DD2F) and hadron-quark (DD2F-SF5) EOS, respectively. In the left panel of Fig. 1 we see the clear growth and eventual dominance of the C_1 mode on dynamical timescales, which is indicative of the development of the one-armed spiral instability. On the other hand, the right panel of Fig. 1 clearly shows that the C_1 mode never dominates the fluid evolution, suggesting a suppression of that density mode relative to the analogous hadronic case depicted in the left panel.

In the left panel of Fig. 2 we show the energy carried by the $\ell=2, m=1$ GW mode as a function of time for simulations employing the DD2F (hadronic) and DD2F-SF5 (hybrid hadron-quark) EOSs. We find that the energy carried in the $\ell=2$, $m=1$ mode of the GWs is significantly smaller in the simulation employing a hybrid hadron-quark EOS, indicating that the one-armed spiral

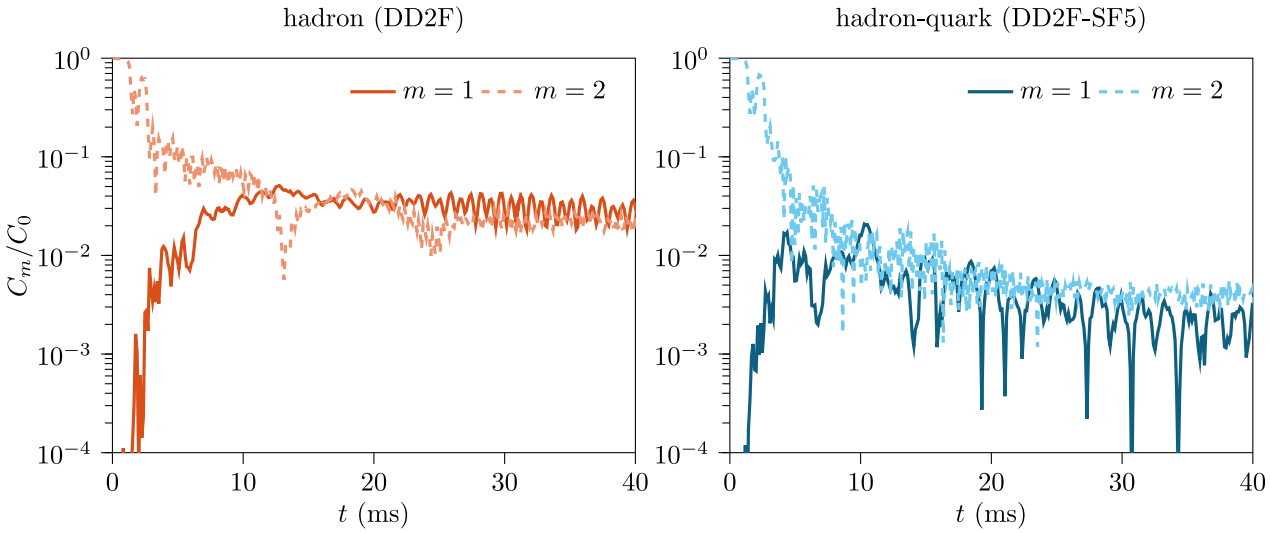

FIG. 1. Left panel: Density mode decomposition following Eq. (2) for a simulation which employs a purely hadronic EOS (DD2F). We depict the dominant density modes (C_2 and C_1) scaled by the C_0 mode to show the relative strength of each fluid pattern. Right panel: Same as the left panel but for a simulation which employs an EOS with a hadron-quark PT (DD2F-SF5, which is identical to the hadronic DD2F model below the threshold densities for the phase transition).

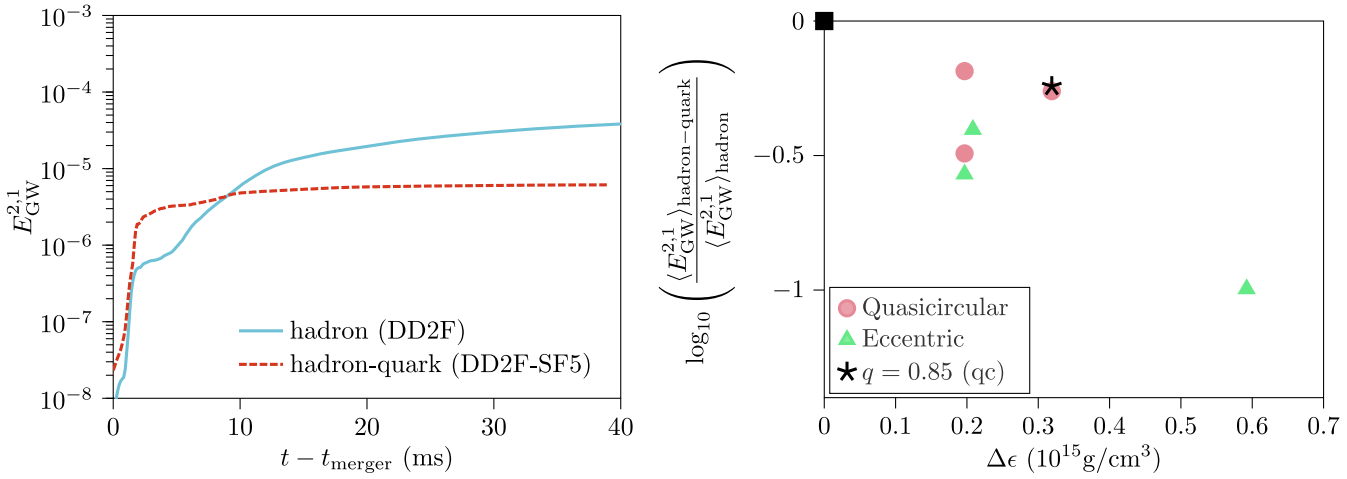

FIG. 2. Left panel: Energy carried by GWs in the $\ell = 2, m = 1$ mode as a function of time. The development of the one-armed spiral instability can be observed in the purely hadronic simulation, as the energy in the $\ell = 2, m = 1$ GW mode continues to grow, but is suppressed in the hadron-quark simulation. Right panel: Time-averaged energy emitted by GWs in the $\ell = 2, m = 1$ mode, normalized by the same quantity for the corresponding hadronic EOS, as a function of the energy density gap separating the hadronic and quark phases. We depict results for quasicircular and eccentric mergers with pink triangles and green circles, respectively. We find that the energy emitted by the $\ell = 2, m = 1$ GW mode decreases by up to approximately an order of magnitude for larger energy density gaps.

instability is relatively suppressed in scenarios with deconfinement PTs at densities relevant for BNS mergers. We emphasize that in Fig. 1 and in the left panel of Fig. 2 we showcase results for a set of EOS models which are identical below the threshold for a PT, and as such the simulations have identical initial conditions. We find that this relative suppression exists for all of our simulations, regardless of initial condition, modeling assumptions as listed in Table II, or pair of EOS models considered.

In the right panel of Fig. 2, we show the time-averaged energy emitted by the $\ell = 2, m = 1$ GW mode $\langle E^{2,1}_{\rm GW}\rangle$ as a function of the energy density gap $\Delta\epsilon$ for all of our simulations. For the results depicted in the right panel of Fig. 2, we time average over a window of $\Delta t \approx 40$ ms after the merger except for cases that lead to a remnant collapse on shorter timescales (in such cases, we time average until the collapse of the NS remnant). To account for differences and uncertainties in the hadronic sector of the NS EOS, we normalize all data by that corresponding to a complementary simulation that uses identical initial data and modeling assumptions but employs a purely hadronic EOS having the same low-density behavior below the PT threshold as the hybrid hadron-quark EOS. As such, we depict the point corresponding to all hadronic EOS simulations with a black square at $\Delta\epsilon = 0$. Each simulation is time averaged to the same extent as its complementary hadronic simulation. The scatter of data suggest a potential anticorrelation between the energy carried in the $\ell = 2, m = 1$ GW mode and the size of the energy density gap, although we note significant variability in the trend. Our findings suggest that as the size of the energy density gap (and thereby the qualitative "strength" of the PT) increases, GW emission in the $\ell = 2, m = 1$ mode decreases; the simulation employing the strongest PT leads to a relative suppression in $\langle E^{2,1}_{\rm GW}\rangle$ of approximately an order of magnitude.

Note that in Fig. 2 we also show the relative suppression of the GW energy in the $\ell = 2, m = 1$ mode, but for the case of a system with mass ratio $q = 0.85$, marked with a black star marker. The datum for the pair of unequal mass ratio simulations shown in Fig. 2 demonstrates that there is significant agreement in the relative suppression of the one-armed spiral instability between the unequal mass ratio and equal mass ratio cases at the same value of $\Delta\epsilon$. Specifically, we find that there is only a 3% difference in the relative growth of $E^{2,1}_{\rm GW}$ between the unequal and equal mass ratio cases of the same $\Delta\epsilon$. In principle, the one-armed spiral instability is expected to be seeded at a stronger level for systems with $q \neq 1$. However, in this work we consider the effect of deconfinement on the development of the one-armed spiral instability PTs, relative to cases with identical initial conditions and modeling assumptions that employ purely hadronic EOSs. As such, system properties such as the mass ratio and other modeling assumptions are expected to cancel out between comparison cases; the only difference between the simulations which we compare is whether or not the EOS contains a deconfinement PT to quark matter.

As the present work is the first ever to report the potential relative suppression of the one-armed spiral instability due to deconfinement PTs, a significant amount of work remains to be done to understand whether the potential anticorrelation suggested by the right panel of Fig. 2 is robust, including the consideration of EOS models that more finely sample the parameter space of $\Delta\epsilon$ and a further investigation of the effects of system properties such as the mass ratio. We leave such investigations to future work.

V. DISCUSSION AND CONCLUSION

The characteristic frequency associated with peak emission in the $\ell = 2, m = 1$ GW mode has half the value of that associated with the $\ell = 2$, $m = 2$ mode (i.e., $f^{2,1}_{\rm peak} = f^{2,2}_{\rm peak}/2$). Observationally, a GW signal would contain information at all contributing frequencies. However, the dominant GW emission associated with binary coalescence is always expected to be from the $\ell = 2, m = 2$ contribution, such that $f_{\rm peak} = f^{2,2}_{\rm peak}$. Therefore, a potential observational signature of the one-armed spiral instability is the growth in power of an incoming GW signal at a frequency that is half of the dominant frequency; if it develops in the postmerger environment, the one-armed spiral instability will continuously power the emission of GWs at $f_{\rm peak}/2$, while emission in the dominant $f_{\rm peak}$ decays in time [86].

In Fig. 3 we show the postmerger GW amplitude spectrum density (ASD) for a symmetric, edge-on binary situated at a distance of 40 Mpc, which is consistent with the luminosity distance observed for GW170817 [87]. The edge-on configuration is the most optimal for the detection of an $m = 1$ mode. As expected, we see a relative suppression of power in the $m = 1$ mode (with respect to the complementary hadronic simulation) with the onset of a deconfinement PT. In this configuration, the appearance of quarks in the post-merger remnant results in a relative suppression of the postmerger signal-to-noise ratio (SNR) of the $(\ell = 2, m = 1)$ mode by a factor of 2, from 2.14 in the hadronic case to 1.08 in the hadron-quark case in the 40 km Cosmic Explorer detector [42]. The GW ASD peak of the $\ell = 2$, $m = 1$ mode (between 1–2 kHz) and the postmerger ASD peak of the $\ell = 2$, $m = 2$ mode (between 2–4 kHz), lie, respectively, in the most sensitive regions of the 40 km and the 20 km postmerger optimized Cosmic Explorer configurations. Our analysis recommends an increase in detector sensitivities in the high-frequency regimes (see also [88]) for best possible constraints on deconfinement PTs in BNS mergers, within the context of multimodal GW spectroscopy. In cases where the one-armed spiral instability develops, all binary inclinations except directly face on will produce GWs with a $l = 2$, $m = 1$ component. The one-armed spiral instability leads to a unique bimodal GW spectrum where the two most dominant peaks correspond exactly to $f_{\rm peak}$ and $f_{\rm peak}/2$. As such, a superposition of all signal modes may still in principle be used to extract the relative strength of the one-armed spiral instability. For instance, the SNR of a postmerger GW signal can be measured in a range of frequencies up to the inferred $f_{\rm peak}$; in cases where the one-armed spiral instability develops the dominant contribution to the signal in this range of frequencies is expected to be from the $l = 2$, $m = 1$ mode for all inclinations except directly face on. We note that the only way to completely remove the $l = 2$, $m = 1$ mode from the signal is in the highly specific scenario of an equal mass, directly face on binary. Given reasonable expectations for distributions in the inclination and mass ratio of BNS systems, we may typically expect a contribution from the $l = 2$, $m = 1$ mode. However, deconfinement PTs may act to suppress the instability. In other words, except for the highly specific scenario of a face-on $q = 1$ binary, the lack of significant SNR over $f_{\rm peak}/2$ may be used to constrain the high-density

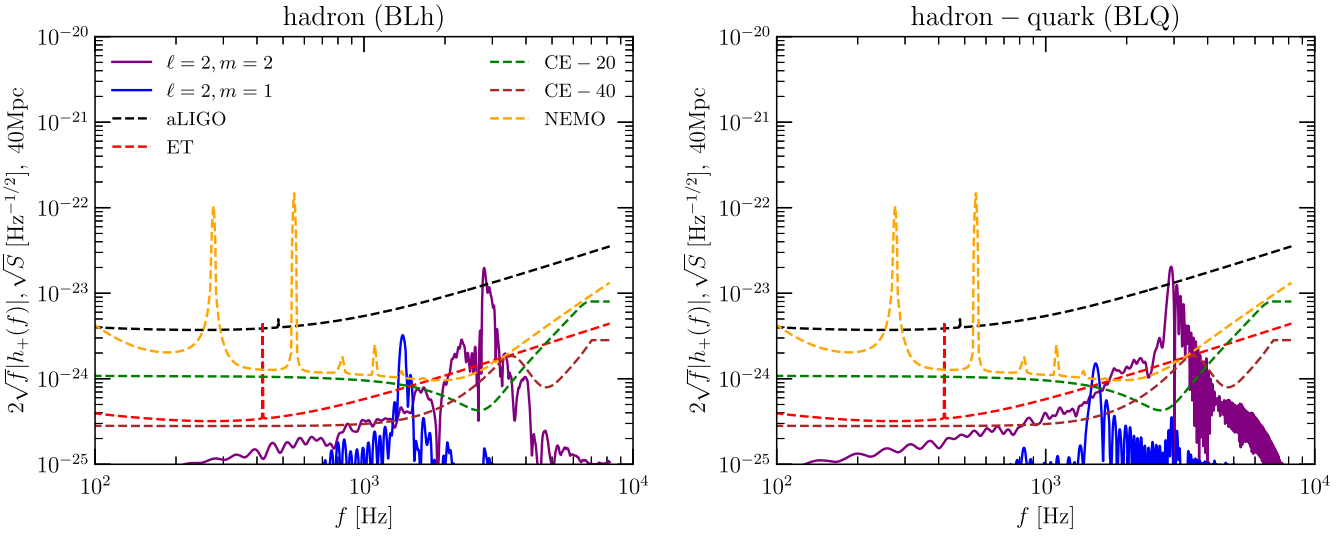

FIG. 3. Multimodal GW amplitude spectrum computed for symmetric binaries of total mass $M = 2.6 M_\odot$ in an edge-on configuration. Also shown are the noise sensitivity curves for advanced LIGO (aLIGO), Einstein Telescope (ET), the 20 km postmerger-optimized configuration for the Cosmic Explorer (CE20), and the 40 km configuration for Cosmic Explorer (CE40). A suppression in the amplitude spectral density as a result of the deconfinement PT may be detectable with the third generation detectors and most cleanly with CE40.

EOS as highlighted by our work. For further detail on the detectability of the one-armed spiral instability via GW spectroscopy, we refer the reader to [77].

In [15] it was established that quasiuniversal relations in the value of $f_{\rm peak}$ may be established for hadronic EOS models, and that EOS models which include a deconfinement PT unambiguously deviate from such universal relations (although recent work suggests that EOS features other than phase transitions may be responsible for deviations away from these quasiuniversal relations [89]). As it is not presently understood whether similar relations exist in a quantity that measures the strength of the one-armed spiral instability (such as $\langle E^{2,1}_{\rm GW}\rangle$), we cannot establish whether the hadron-quark EOS models considered in this work deviate from such hypothetical quasiuniversal relations. We may instead consider the effect showcased in this work as an additional tool to infer the presence and nature of PTs in BNS mergers. For example, when considered in combination with other known effects of PTs on BNS merger observables such as $f_{\rm peak}$ [15] and the associated kilonova (KN) brightness [27], the measurement of SNR$(f_{\rm peak}/2)$ (which is directly proportional to $\langle E^{2,1}_{\rm GW}\rangle$ as considered in our work) may allow for significant constraints on properties of the deconfinement PT. In principle the effects we discuss in this paper may be conflated with the effects of relatively soft EOS models [77] or potentially other effects such as nonconvexity in the EOS [89]. In order to state definitively whether deconfinement PTs have a comparable effect on the one-armed spiral instability as relatively soft EOSs, we would need to consider hadronic EOS models over a significantly wider range of stiffness. Such a study would help establish whether quasiuniversal relations exist in $\langle E^{2,1}_{\rm GW}\rangle$ or comparable metrics for the strength of the one-armed spiral instability in the case of hadronic EOSs, which we could then use as a standard against which to compare the effects presented in our work. We leave the investigation of quasiuniversal relations for the strength of the one-armed spiral instability to future work.

In this work we have highlighted, for the first time, that high-density deconfinement PTs may act to relatively suppress the one-armed spiral instability. We find an anticorrelation between the energy carried in the $\ell = 2$, $m = 1$ GW mode and the size of the energy density gap that qualitatively separates the hadronic and quark phases. Our findings reveal a potential deep connection between observable multimodal GW emission and the microphysical description of matter in the postmerger environment. We expect the one-armed spiral instability to be detectable at distances of 40 Mpc using future generation detectors [77]. If evidence of a strong one-armed spiral mode can be inferred from GW observations of the post-BNS merger environment, our findings suggest that a strong high-density deconfinement PT at the densities relevant to BNS mergers would be disfavored. On the other hand, if evidence for the one-armed spiral instability is not found for close-by BNS mergers, this could also point to the possibility of a deconfinement PT taking place at densities relevant to BNS mergers.

Similar studies considering the effect of PTs on BNS GW observables have not observed the relative suppression reflected in our simulations. For example, the Appendix of [35] considers a single comparison between a simulation with hadronic degrees of freedom and a hadron-quark PT. There, they show a potential relative amplification of the GW amplitude in the $\ell = 2$, $m = 1$ mode when allowing for a hadron-quark PT. However, that single comparison scenario is markedly different from those considered in this work. Specifically, in [35] the PT only occurs $t = 3$–4 ms after the merger, whereas the PT occurs within $t \approx 0.5$ ms for the simulations in this work. As such, the early development of the instability may not be impacted by the PT in the scenario considered in [35]. Moreover, we note that in our study we consider the time averaged GW energy carried in the $l = 2$, $m = 1$ mode. Without comparing the same quantities used in our study to understand the development of the one-armed spiral, it is impossible to say whether the single comparison considered in [35] is contrary to the trend depicted in Fig. 2. Finally, we emphasize that [35] considers coarser numerical grids than our study for the single relevant comparison (a roughly 30% coarser numerical grid when compared to the standard resolution simulations in our work, which is consistent with our LR simulations), and does not consider an exploration of relevant effects as was done in our study (e.g., the size of $\Delta\epsilon$ and different phase constructions). Importantly, the authors of [35] do not establish that their simulations, in the context of the one armed spiral instability, are in the convergent regime, as the amplification of the $\ell = 2$, $m = 1$ after a hadron-quark PT occurs in the remnant reported in that work is not observed using higher resolution simulations. As such, it remains unclear whether the potential deviation of that result from the trend established in Fig. 2 is not due to relatively higher numerical error in [35]. In the Appendix we discuss the complexity of understanding fluid instabilities in BNS mergers using LR grids.

Binary neutron star mergers with nonunity mass ratios are in principle more generic and common than the equal mass ratio systems considered in this work. Moreover, the inherent asymmetry in unequal mass ratio mergers may provide a reliable mechanism for efficiently seeding the one-armed spiral instability after the merger and has been shown to result in a stronger, faster development of the instability [78]. Although we present only a single case study for cases with unequal mass ratios in the present work, we find support for our main claim (that high-density deconfinement PTs may suppress the development of the one-armed spiral instability when compared to analogous cases with purely hadronic degrees of freedom) there as well. Due to the scope of the present work and the increased parameter space when considering unequal mass ratio cases, we find that a more systematic consideration of unequal mass ratio cases than can be presented in here is

warranted. As such, we leave a full investigation of the effects of unequal mass ratio to future studies. We point out that other effects relevant in the postmerger environment—such as the presence of strong magnetic fields [90] and additional degrees of freedom that can cause a sudden softening of the EOS—may affect the development of the one-armed spiral instability. However, the relevant timescales and extent to which the aforementioned phenomena can affect the development of nonaxisymmetric instabilities or the GW spectrum remains uncertain [77,91], and may not impact our conclusions [92,93]. The effects discussed in the present work arise on dynamical timescales $\sim\mathcal{O}(10\ \mathrm{ms})$ and may be the dominant mechanism for the relative suppression of the one-armed spiral instability. Additionally, although we find a trend in the decrease of energy carried by the $\ell = 2, m = 1$ GW mode for larger values of $\Delta\epsilon$, additional studies will help establish a more robust trend and provide an understanding of the potential spread in the trend. In particular, future lines of investigation will include the following: (1) considering the combined effects of the mass ratio and high-density PTs on the development of the one-armed spiral instability to a greater extent than could be done in this work; (2) considering the effects of accurate neutrino transport on high-density deconfinement PTs, as neutrinos may modify the composition of matter and thereby potentially affect the onset of the PT; (3) employing EOS models at systematically increasing values of $\Delta\epsilon$ while holding the hadronic region of the EOS fixed, as a limitation of the present work is the assumption that the $\ell = 2, m = 1$ GW mode is perfectly known in the case of hadronic EOSs; and (4) investigating the effects discussed in this work in scenarios with a crossover to quark matter, as our present work only considers EOS models with phase transitions. We leave such studies to future work.

ACKNOWLEDGMENTS

P. E. acknowledges funding from the National Science Foundation under Grant No. PHY-2020275. D. R. acknowledges funding from the U.S. Department of Energy, Office of Science, Division of Nuclear Physics under Award No. DE-SC0021177 and from the National Science Foundation under Grants No. PHY-2011725, No. PHY-2116686, and No. AST-2108467. Simulations were performed on Bridges2 and Expanse (Grant No. NSF XSEDE allocation TG-PHY160025). This research used resources of the National Energy Research Scientific Computing Center, a DOE Office of Science User Facility supported by the Office of Science of the U.S. Department of Energy under Contract No. DE-AC02-05CH11231.

APPENDIX: ON THE EFFECTS OF GRID RESOLUTION

Our main diagnostic for monitoring the development of the one-armed spiral instability is the energy carried in the $\ell = 2$, $m = 1$ mode of the GWs, which we further discuss in Sec. IV B. We find that for most cases in our study, the relative suppression of the one armed spiral instability is observed at lower grid resolutions. However, there are notable exceptions for two pairs of simulations at lower resolutions. Specifically, we find that the LR versions for two of our simulations that employ high-density deconfinement phase transitions do not show a relative suppression of $\langle E^{2,1}_{\mathrm{GW}}\rangle$, but instead a relative growth with respect to the analogous simulations employing a purely hadronic EOS. These cases seemingly contradict the discussion in the main text and are more consistent with the single case study showcased in [35]. However, we note that grid effects are crucial in determining the growth and saturation of the one-armed spiral instability. Specifically, the one-armed spiral instability may be seeded in a variable nature in the context of numerical studies. Unless it is explicitly excited as a nonaxisymmetric perturbation of a known amplitude (e.g., as a fixed-amplitude perturbation in the rest mass density), the one-armed spiral instability arises numerically from error at the level of floating-point precision [94]. As such, small differences in the early postmerger evolution of the fluid can result in the instability being seeded at different strengths; this is potentially affected most strongly by the grid resolution. We do not explicitly seed the one-armed spiral instability using fluid perturbations in this work and, as a result, simulations that either run on different machines or use different grid resolutions libraries may result in different strengths for the initial instability seed.

To discuss the relative strength of the one-armed spiral instabilities across simulations which employ different grid structures, we consider $E^{2,1}_{\mathrm{GW}}$ normalized to its value at a time shortly after the merger; we depict normalized quantities because of the variable nature in which the one-armed spiral instability is seeded in the immediate postmerger environment in the context of numerical studies. In Fig. 4 we show the energy in the $\ell = 2, m = 1$ GW mode $E^{2,1}_{\mathrm{GW}}$ as a function of time for a set of low resolution simulations. The left panel of Fig. 4 shows $E^{2,1}_{\mathrm{GW}}$ as extracted from our simulations and appears to show that the simulation employing a hadron-quark EOS produces a larger energy in the $\ell = 2, m = 1$ GW mode. However, it is clear that the energy at a time shortly after the merger $E^{2,1}_{\mathrm{GW}}(t_{\mathrm{merger}} + \tau_\epsilon)$ (where τ_ϵ is a small additive time) is larger for the hadron-quark simulation, suggesting that the one-armed spiral instability was seeded at a larger amplitude in that case. In order to account for the different levels at which the one-armed spiral instability is seeded in the immediate postmerger environment, we normalize the quantities used to diagnose the relative strength of the instability at a time shortly after the merger $t_{\mathrm{norm}} = t_{\mathrm{mer}} + \tau_\epsilon$. We find that setting $\tau_\epsilon = 0.5$ ms results in all simulations in our work having roughly equal values of $E^{2,1}_{\mathrm{GW}}$ in the few ms immediately following merger. We find that setting τ_ϵ between 0.1 and 1 ms ensures that all simulations have approximate equality in the level

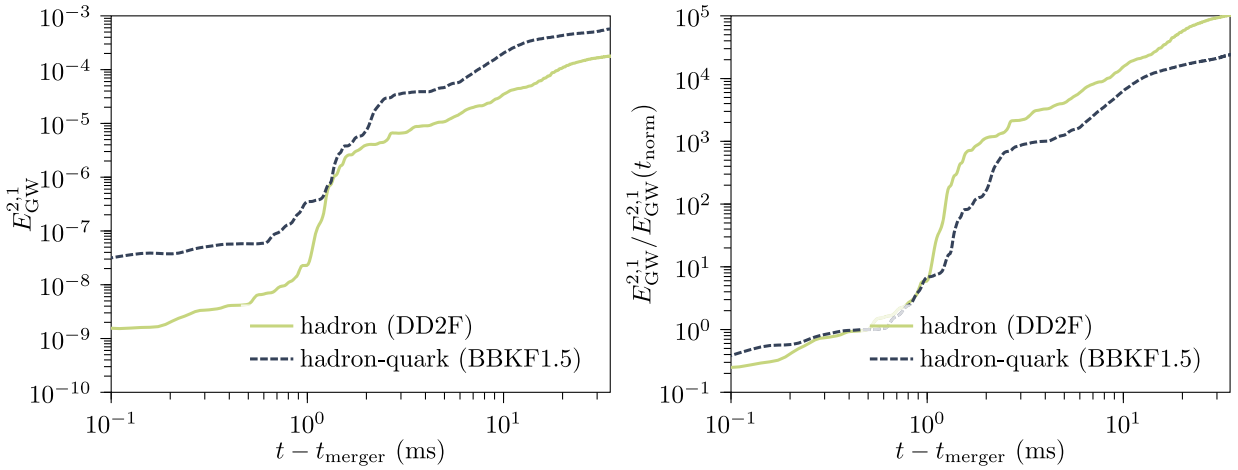

FIG. 4. Left panel: Energy in the $\ell = 2, m = 1$ GW mode as a function of time for simulations employing a hadronic (DD2F) and hadron-quark (BBKF1.5) EOS; the simulations use identical initial conditions and are run with a grid resolution of $\Delta x = 369.2$ m in the finest grid. These results showcase that the one-armed spiral instability may be seeded at different levels in the postmerger environment for different simulations. Right panel: Same quantity as the left panel, but normalized to the value at a time shortly after merger, $t_{\rm norm} = t_{\rm merger} + 0.5$ ms. Normalizing at this time accounts for the one-armed spiral instability being seeded at disparate levels across simulations.

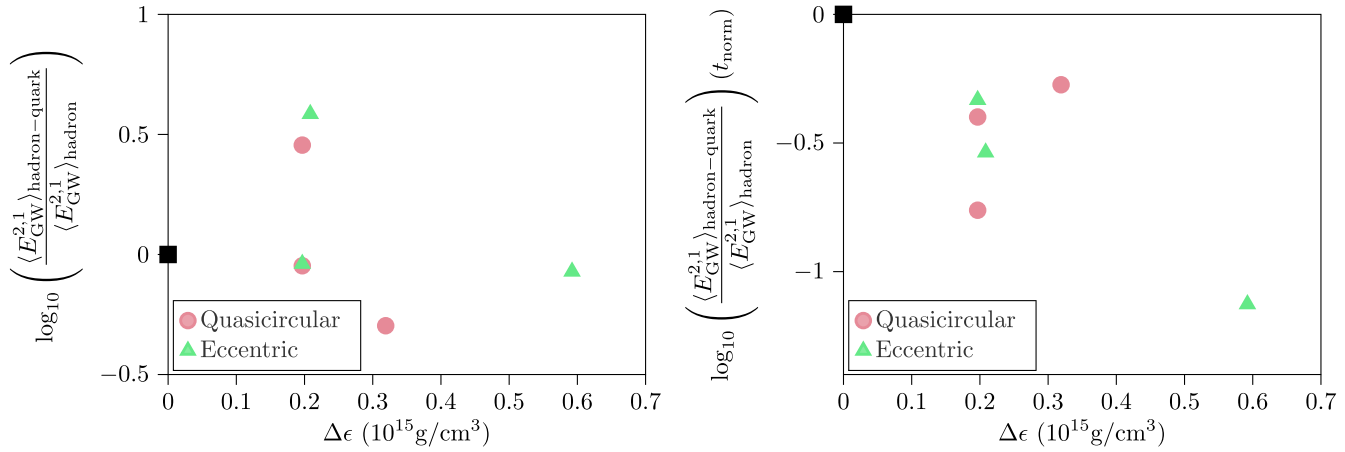

FIG. 5. Left panel: Time-averaged energy emitted by GWs in the $\ell = 2$, $m = 1$ mode, normalized by the same quantity for the complementary hadronic EOS, as a function of the energy density gap separating the hadronic and quark phases. We show results for the LR simulations in our work. Right panel: Same as the left panel, but normalizing all data at a time shortly after merger, $t_{\rm norm} = t_{\rm merger} + 0.5$ ms as consistent with Fig. 4.

at which the one-armed spiral instability is seeded, regardless of grid resolution or computational hardware used. We emphasize that our results at higher resolution are observed without the aforementioned normalization, but considering the normalization allows us to more suitably compare the development of the one-armed spiral instability across different grid resolutions. In Fig. 5 we show the time-averaged GW energy carried in the $l = 2, m = 1$ mode as a function of $\Delta\epsilon$ for all LR simulations in our work. We find that without accounting for disparate levels of the instability seed (left panel of Fig. 5), our data does not closely follow the potential trend established by the SR simulations in Fig. 2. However, normalizing all LR simulation data at a time consistent with Fig. 4 results in a much closer scatter of data between the LR and SR sets (right panel of Fig. 5). We leave the investigation of grid resolution effects, as well as the consideration of even higher resolution grids than could be included in this study, to future work.

[1] A. Perego, S. Bernuzzi, and D. Radice, Eur. Phys. J. A **55**, 124 (2019).
[2] M. Shibata, Phys. Rev. Lett. **94**, 201101 (2005).
[3] T. Hinderer, B. D. Lackey, R. N. Lang, and J. S. Read, Phys. Rev. D **81**, 123016 (2010).
[4] T. Damour, A. Nagar, and L. Villain, Phys. Rev. D **85**, 123007 (2012).
[5] Y. Sekiguchi, K. Kiuchi, K. Kyutoku, and M. Shibata, Phys. Rev. Lett. **107**, 211101 (2011).
[6] K. Hotokezaka, K. Kyutoku, H. Okawa, M. Shibata, and K. Kiuchi, Phys. Rev. D **83**, 124008 (2011).
[7] A. Bauswein, T. W. Baumgarte, and H. T. Janka, Phys. Rev. Lett. **111**, 131101 (2013).
[8] D. Radice, S. Bernuzzi, W. Del Pozzo, L. F. Roberts, and C. D. Ott, Astrophys. J. Lett. **842**, L10 (2017).
[9] B. P. Abbott *et al.* (LIGO Scientific and Virgo Collaborations), Astrophys. J. Lett. **851**, L16 (2017).
[10] B. Margalit and B. D. Metzger, Astrophys. J. Lett. **850**, L19 (2017).
[11] A. Bauswein, O. Just, H.-T. Janka, and N. Stergioulas, Astrophys. J. Lett. **850**, L34 (2017).
[12] D. Radice, A. Perego, F. Zappa, and S. Bernuzzi, Astrophys. J. Lett. **852**, L29 (2018).
[13] E. R. Most, L. J. Papenfort, V. Dexheimer, M. Hanauske, S. Schramm, H. Stöcker, and L. Rezzolla, Phys. Rev. Lett. **122**, 061101 (2019).
[14] E. R. Most, L. Jens Papenfort, V. Dexheimer, M. Hanauske, H. Stoecker, and L. Rezzolla, Eur. Phys. J. A **56**, 59 (2020).
[15] A. Bauswein, N.-U. F. Bastian, D. B. Blaschke, K. Chatziioannou, J. A. Clark, T. Fischer, and M. Oertel, Phys. Rev. Lett. **122**, 061102 (2019).
[16] M. W. Coughlin, T. Dietrich, B. Margalit, and B. D. Metzger, Mon. Not. R. Astron. Soc. **489**, L91 (2019).
[17] S. De, D. Finstad, J. M. Lattimer, D. A. Brown, E. Berger, and C. M. Biwer, Phys. Rev. Lett. **121**, 091102 (2018); **121**, 259902(E) (2018).
[18] B. P. Abbott *et al.* (LIGO Scientific and Virgo Collaborations), Phys. Rev. X **9**, 011001 (2019).
[19] B. P. Abbott *et al.* (LIGO Scientific and Virgo Collaborations), Phys. Rev. Lett. **121**, 161101 (2018).
[20] D. Radice and L. Dai, Eur. Phys. J. A **55**, 50 (2019).
[21] T. Dietrich, M. W. Coughlin, P. T. H. Pang, M. Bulla, J. Heinzel, L. Issa, I. Tews, and S. Antier, Science **370**, 1450 (2020).
[22] M. Breschi, A. Perego, S. Bernuzzi, W. Del Pozzo, V. Nedora, D. Radice, and D. Vescovi, Mon. Not. R. Astron. Soc. **505**, 1661 (2021).
[23] M. Breschi, S. Bernuzzi, D. Godzieba, A. Perego, and D. Radice, Phys. Rev. Lett. **128**, 161102 (2022).
[24] R. Kashyap *et al.*, Phys. Rev. D **105**, 103022 (2022).
[25] A. Perego, D. Logoteta, D. Radice, S. Bernuzzi, R. Kashyap, A. Das, S. Padamata, and A. Prakash, Phys. Rev. Lett. **129**, 032701 (2022).
[26] Y. Fujimoto, K. Fukushima, K. Hotokezaka, and K. Kyutoku, Phys. Rev. Lett. **130**, 091404 (2023).
[27] A. Prakash, D. Radice, D. Logoteta, A. Perego, V. Nedora, I. Bombaci, R. Kashyap, S. Bernuzzi, and A. Endrizzi, Phys. Rev. D **104**, 083029 (2021).
[28] C. D. Capano, I. Tews, S. M. Brown, B. Margalit, S. De, S. Kumar, D. A. Brown, B. Krishnan, and S. Reddy, Nat. Astron. **4**, 625 (2020).
[29] P. T. H. Pang, I. Tews, M. W. Coughlin, M. Bulla, C. Van Den Broeck, and T. Dietrich, Astrophys. J. **922**, 14 (2021).
[30] E. Annala, T. Gorda, E. Katerini, A. Kurkela, J. Nättilä, V. Paschalidis, and A. Vuorinen, Phys. Rev. X **12**, 011058 (2022).
[31] E. Loffredo, A. Perego, D. Logoteta, and M. Branchesi, Astron. Astrophys. **672**, A124 (2023).
[32] D. Logoteta, Universe **7**, 408 (2021).
[33] M. Evans *et al.*, arXiv:2109.09882.
[34] A. Lovato *et al.*, arXiv:2211.02224.
[35] L. R. Weih, M. Hanauske, and L. Rezzolla, Phys. Rev. Lett. **124**, 171103 (2020).
[36] S. Blacker, N.-U. F. Bastian, A. Bauswein, D. B. Blaschke, T. Fischer, M. Oertel, T. Soultanis, and S. Typel, Phys. Rev. D **102**, 123023 (2020).
[37] A. Kedia, H. I. Kim, I.-S. Suh, and G. J. Mathews, Phys. Rev. D **106**, 103027 (2022).
[38] S. L. Liebling, C. Palenzuela, and L. Lehner, Classical Quantum Gravity **38**, 115007 (2021).
[39] S. Tootle, C. Ecker, K. Topolski, T. Demircik, M. Jarvinen, and L. Rezzolla, SciPost Phys. **13**, 109 (2022).
[40] A. Bauswein, S. Blacker, V. Vijayan, N. Stergioulas, K. Chatziioannou, J. A. Clark, N.-U. F. Bastian, D. B. Blaschke, M. Cierniak, and T. Fischer, Phys. Rev. Lett. **125**, 141103 (2020).
[41] A. Bauswein, S. Blacker, G. Lioutas, T. Soultanis, V. Vijayan, and N. Stergioulas, Phys. Rev. D **103**, 123004 (2021).
[42] D. Reitze *et al.*, Bull. Am. Astron. Soc. **51**, 035 (2019).
[43] M. Punturo *et al.*, Classical Quantum Gravity **27**, 194002 (2010).
[44] K. Ackley *et al.*, Pub. Astron. Soc. Aust. **37**, e047 (2020).
[45] M. G. Alford and S. Han, Eur. Phys. J. A **52**, 62 (2016).
[46] V. Paschalidis, K. Yagi, D. Alvarez-Castillo, D. B. Blaschke, and A. Sedrakian, Phys. Rev. D **97**, 084038 (2018).
[47] D. E. Alvarez-Castillo and D. B. Blaschke, Phys. Rev. C **96**, 045809 (2017).
[48] M. Alford and A. Sedrakian, Phys. Rev. Lett. **119**, 161104 (2017).
[49] G. Bozzola, P. L. Espino, C. D. Lewin, and V. Paschalidis, Eur. Phys. J. A **55**, 149 (2019).
[50] P. L. Espino and V. Paschalidis, Phys. Rev. D **105**, 043014 (2022).
[51] J. S. Read, B. D. Lackey, B. J. Owen, and J. L. Friedman, Phys. Rev. D **79**, 124032 (2009).
[52] N.-U. F. Bastian, Phys. Rev. D **103**, 023001 (2021).
[53] I. Bombaci and D. Logoteta, Astron. Astrophys. **609**, A128 (2018).
[54] D. Logoteta, A. Perego, and I. Bombaci, Astron. Astrophys. **646**, A55 (2021).
[55] J. W. York, Jr., Phys. Rev. Lett. **82**, 1350 (1999).
[56] E. Gourgoulhon, P. Grandclement, K. Taniguchi, J.-A. Marck, and S. Bonazzola, Phys. Rev. D **63**, 064029 (2001).
[57] K. Taniguchi, E. Gourgoulhon, and S. Bonazzola, Phys. Rev. D **64**, 064012 (2001).
[58] K. Taniguchi and E. Gourgoulhon, Phys. Rev. D **65**, 044027 (2002).

[59] D. Radice, F. Galeazzi, J. Lippuner, L. F. Roberts, C. D. Ott, and L. Rezzolla, Mon. Not. R. Astron. Soc. **460**, 3255 (2016).

[60] D. Radice and L. Rezzolla, Astron. Astrophys. **547**, A26 (2012).

[61] D. Radice, L. Rezzolla, and F. Galeazzi, Mon. Not. R. Astron. Soc. **437**, L46 (2014).

[62] D. Radice, L. Rezzolla, and F. Galeazzi, Classical Quantum Gravity **31**, 075012 (2014).

[63] D. Pollney, C. Reisswig, E. Schnetter, N. Dorband, and P. Diener, Phys. Rev. D **83**, 044045 (2011).

[64] Y. Zlochower *et al.*, The Einstein Toolkit, (2022), to find out more, visit http://einsteintoolkit.org.

[65] E. Schnetter, S. H. Hawley, and I. Hawke, Classical Quantum Gravity **21**, 1465 (2004).

[66] D. Radice, A. Perego, K. Hotokezaka, S. A. Fromm, S. Bernuzzi, and L. F. Roberts, Astrophys. J. **869**, 130 (2018).

[67] D. Radice, S. Bernuzzi, and A. Perego, Annu. Rev. Nucl. Part. Sci. **70**, 95 (2020).

[68] D. Radice, S. Bernuzzi, A. Perego, and R. Haas, Mon. Not. R. Astron. Soc. **512**, 1499 (2022).

[69] D. Radice, Astrophys. J. Lett. **838**, L2 (2017).

[70] B. K. Pickett, R. H. Durisen, and G. A. Davis, Astrophys. J. **458**, 714 (1996).

[71] J. M. Centrella, K. C. B. New, L. L. Lowe, and J. D. Brown, Astrophys. J. Lett. **550**, L193 (2001).

[72] M. Saijo, T. W. Baumgarte, and S. L. Shapiro, Astrophys. J. **595**, 352 (2002).

[73] S. Ou and J. Tohline, Astrophys. J. **651**, 1068 (2006).

[74] V. Paschalidis, W. E. East, F. Pretorius, and S. L. Shapiro, Phys. Rev. D **92**, 121502 (2015).

[75] W. E. East, V. Paschalidis, and F. Pretorius, Classical Quantum Gravity **33**, 244004 (2016).

[76] W. E. East, V. Paschalidis, F. Pretorius, and S. L. Shapiro, Phys. Rev. D **93**, 024011 (2016).

[77] D. Radice, S. Bernuzzi, and C. D. Ott, Phys. Rev. D **94**, 064011 (2016).

[78] L. Lehner, S. L. Liebling, C. Palenzuela, and P. M. Motl, Phys. Rev. D **94**, 043003 (2016).

[79] C. D. Ott, S. Ou, J. E. Tohline, and A. Burrows, Astrophys. J. Lett. **625**, L119 (2005).

[80] T. Kuroda, T. Takiwaki, and K. Kotake, Phys. Rev. D **89**, 044011 (2014).

[81] R. Kashyap, R. Fisher, E. García-Berro, G. Aznar-Siguán, S. Ji, and P. Lorén-Aguilar, Astrophys. J. **800**, L7 (2015).

[82] R. Kashyap, R. Fisher, E. García-Berro, G. Aznar-Siguán, S. Ji, and P. Lorén-Aguilar, Astrophys. J. **840**, 16 (2017).

[83] E. Wessel, V. Paschalidis, A. Tsokaros, M. Ruiz, and S. L. Shapiro, Phys. Rev. D **103**, 043013 (2021).

[84] M. Saijo and S. Yoshida, Phys. Rev. D **94**, 084032 (2016).

[85] M. Saijo, Phys. Rev. D **98**, 024003 (2018).

[86] S. Bernuzzi, T. Dietrich, and A. Nagar, Phys. Rev. Lett. **115**, 091101 (2015).

[87] B. P. Abbott *et al.*, Phys. Rev. Lett. **119**, 161101 (2017).

[88] T. Zhang, H. Yang, D. Martynov, P. Schmidt, and H. Miao, Phys. Rev. X **13**, 021019 (2023).

[89] G. Rivieccio, D. Guerra, M. Ruiz, and J. A. Font, Phys. Rev. D **109**, 064032 (2024).

[90] L. Franci, R. De Pietri, K. Dionysopoulou, and L. Rezzolla, Phys. Rev. D **88**, 104028 (2013).

[91] C. D. Muhlberger, F. H. Nouri, M. D. Duez, F. Foucart, L. E. Kidder, C. D. Ott, M. A. Scheel, B. Szilágyi, and S. A. Teukolsky, Phys. Rev. D **90**, 104014 (2014).

[92] C. Palenzuela, R. Aguilera-Miret, F. Carrasco, R. Ciolfi, J. V. Kalinani, W. Kastaun, B. Miñano, and D. Viganò, Phys. Rev. D **106**, 023013 (2022).

[93] F. Zappa, S. Bernuzzi, D. Radice, and A. Perego, arXiv: 2210.11491.

[94] P. L. Espino, V. Paschalidis, T. W. Baumgarte, and S. L. Shapiro, Phys. Rev. D **100**, 043014 (2019).